

Chapter 2

Experimental Techniques

In this chapter we briefly introduce the experimental method—Scanning Tunneling Microscopy—used over the course of this thesis. First we review the main concepts and their theoretical background. Then we give a quick overview of the main experimental techniques like scanning tunneling spectroscopy and manipulation, followed by a short description of the actual setup and the sample preparations used throughout this thesis.

2.1 Scanning Tunneling Microscopy

Scanning Tunneling Microscopy (STM) is an experimental technique in surface physics that allows direct imaging of conducting and semiconducting surfaces on the nanometer scale (Fig. 2.1). By using a local probe, images are acquired in real space complementing other techniques like Low Energy Electron Diffraction (LEED) that work in reciprocal space. Additionally, and more importantly perhaps, the STM provides spatially resolved access to the electronic structure of the sample. Since its development in 1981 [1–3], STM has become a powerful and widely used tool in surface science [4]. Further improvements like low temperature setups allowed the investigation of systems of adsorbates, where a high mobility at room temperature would have eluded scanning, such as single molecules or adatoms. Especially these kind of setups promoted the use of STM not only as an imaging tool but also as means to manipulate the sample in a very precise way, for instance by creating nano-sized structures by moving single atoms and molecules [5, 6] or inducing localized chemical reactions [7].

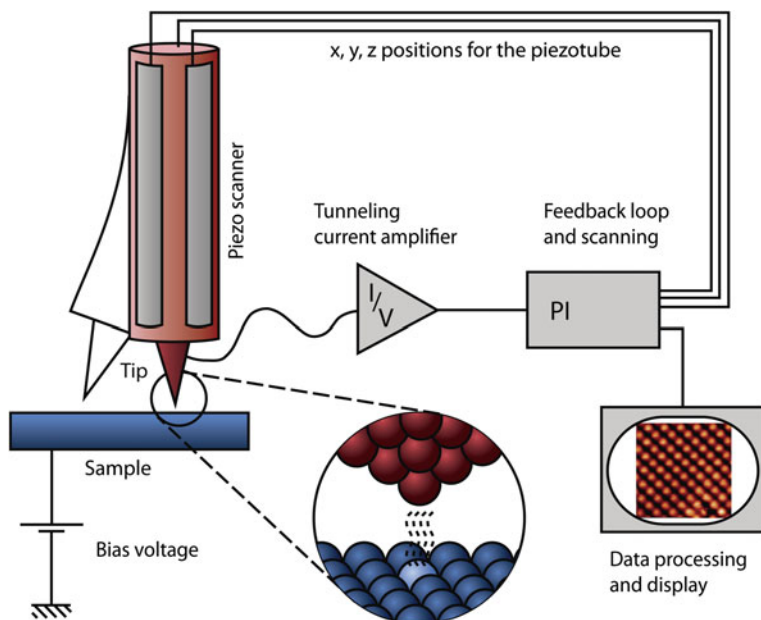


Fig. 2.1 The scanning tunneling microscope: a sharp conducting tip is approached very close ($\sim 5\text{\AA}$) to the sample surface. Due to the bias voltage between tip and sample a current of tunneling electrons can be detected, which depends on the local characteristics of the sample at the position of the tip. Using a piezo electronic actuator the tip is moved in a scanning motion over the sample surface. A topographic image of the surface can be constructed based on the tunneling current signal

2.1.1 The Operating Principle

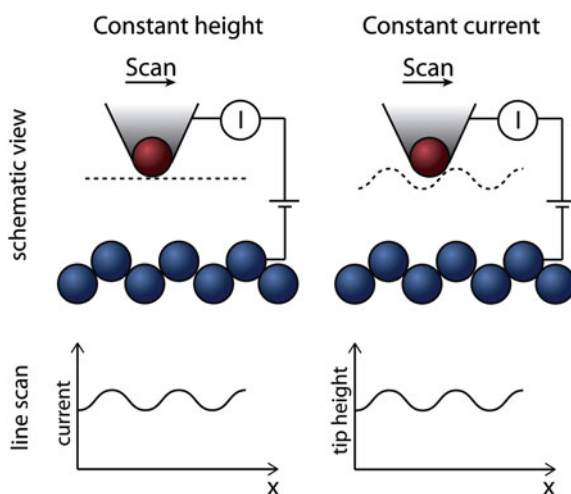
The basic idea of an STM is based on quantum tunneling. Consider a particle with a given energy that is confronted with a barrier in its trajectory. In classical mechanics it cannot cross the barrier if its potential is higher than its own energy. An example of this would be a ball trying to roll up a hill. However, if one looks at a system that is small enough to require a quantum mechanical description, the outcome of this experiment will be different. In quantum mechanics matter is seen as a wave and a particle at the same time. The position and the momentum of an object can only be determined with a certain degree of uncertainty. If the momentum is very sharply defined the position cannot be determined a vice versa, according to the Heisenberg uncertainty principle. This implies that when a quantum mechanical particle faces a potential energy barrier, the probability that the particle crosses the barrier is not zero, but instead decays exponentially over the width of the barrier. Hence, there will always be a small probability for the particle to emerge on the other side of the barrier (see Fig. 2.3). Naturally this probability will depend on the height and width of the barrier.

In an STM this effect is harnessed by approaching a very sharp metallic tip, ideally terminated by just one atom, at a distance of about 0.1–1 nm to a conducting or at least semiconducting sample. The gap between them is the barrier that electrons will tunnel through. In the absence of a bias, both directions for the tunneling from tip to the sample and vice versa are equally probable, and hence no net electron current would be detectable. But when a bias voltage between the sample and the tip is applied one tunneling direction is favored and a measurable current is detected. This tunneling current (typically 1 pA to 10 nA) can be measured and depends exponentially on the distance between the sample and the tip.

Now if the tip scans an area on the surface at a constant height, the current signal is an image of the topography in real space. This is called the constant height scanning mode (see Fig. 2.2). There are some disadvantages to this scanning mode. If the surface has topographic features higher than the scan height, the tip will crash against them, thus changing the surface and the tip. Further, the vertical height of the tip has to be very stable with respect to thermal drift or coupling to external vibrations.

Another more commonly used scanning mode is the constant current mode (see Fig. 2.2). In this case a feedback loop is used to maintain the current constant, by varying the height of the tip, i.e., the tunneling barrier. In this constant current mode the topographic information is recorded in the height control signal during the scan. Because the tip follows the profile of the surface, this mode is better suited for bigger corrugations. In this work the constant current mode was used almost exclusively.

Fig. 2.2 The different STM scanning modes: In constant height mode the tip is scanning at a constant height, the tunneling current signal contains the topographic data. In constant current mode the tunneling current is kept constant by a feedback loop controlling the tip height, the topographic signal is the tip height



2.1.2 Theoretical Descriptions of the Tunneling Process

The tunneling process is described by a variety of different theoretical models. Two of which will be discussed in brief here. The first is a simple time-independent 1D model. Despite its approximative character, this model is very instructive because it can be solved analytically and leads to the fundamental dependencies of the tunneling current. The second model takes all three dimensions into account, as well as the electronic structure of tip and sample.

Simple 1D Model

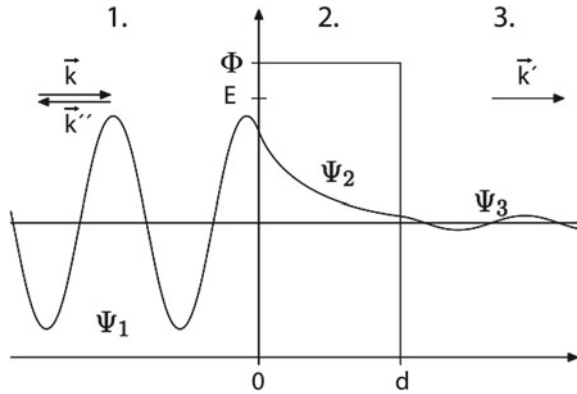
In a first approach the tunnel junction can be modeled as a one dimensional and time independent system. The electron is approximated as a free electron with energy E , separated by a potential barrier of height Φ and thickness d .

The stationary Schrödinger equation (Eq. 2.1) for the electron wave functions Ψ in the tip, the sample, and the barrier has to be solved:

$$\left(\frac{\hbar^2}{2m_e} \Delta + V(r) \right) \Psi = E \Psi \quad (2.1)$$

where m_e is the electron mass, and $V(r)$ the potential describing the barrier with height Φ and width d and E the energy of the electron. The exact solution for these wave functions can be found by using a plane wave ansatz for Ψ for the three regions (tip (1), vacuum (2) and sample (3), see Fig. 2.3).

Fig. 2.3 One-dimensional potential barrier with energy Φ and width d . A particle that is traveling from the left to the right is described by three wavefunctions Ψ before (1), inside (2), and after (3) the barrier. This leads to three wavenumbers \vec{k} , \vec{k}' and \vec{k}'' . The \vec{k}' solution crossed the barrier



$$\begin{aligned}\Psi_1 &= e^{ikz} + A \cdot e^{-ikz} \\ \Psi_2 &= B \cdot e^{i\kappa z} + C \cdot e^{-i\kappa z} \\ \Psi_3 &= D \cdot e^{ikz}\end{aligned}$$

$$\text{with } k = \frac{\sqrt{2m_e E}}{\hbar} \quad \text{and } \kappa = \frac{\sqrt{2m_e(\Phi - E)}}{\hbar}$$

By matching the amplitude and the first derivative at the boundaries of the different potential regions, the coefficients (A, B, C, D) can be determined [8].

We can then define a transmission coefficient T by comparing the wavefunctions on both sides of the barrier:

$$T = \frac{|\Psi_1|^2}{|\Psi_3|^2} = \frac{A^2}{D^2} = \left[\left(\frac{k^2 + \kappa^2}{2k\kappa} \right)^2 \sinh(\kappa d) \right]^{-1} \quad (2.2)$$

which can be simplified for a high barrier potential compared to the energy of the electron $\Phi \gg E$, *i.e.*, if $\kappa d \gg 1$

$$T \approx \frac{16k^2\kappa^2}{(k^2 + \kappa^2)^2} \cdot e^{-2\kappa d} \quad (2.3)$$

The number of tunneling electrons, that is the tunneling current I , will be proportional to T . Therefore with the thickness of the barrier given by the tip height d , we find:

$$I \propto T \propto e^{-2\kappa d} \quad (2.4)$$

We have thus shown that the tunneling current depends exponentially on the tip-sample distance d . The barrier height Φ is the average work function of the sample and tip. For typical values of $\Phi = 5$ eV and $E = 2$ eV, this means a change of one order of magnitude for I for change of 1 Å in the tip sample distance d . This exponential dependency is the underlying mechanism for the high vertical resolution of the STM technique.

The Tersoff-Hamann Model

This model can be extended by including the electronic structure of the tip and sample and the three dimensions of the problem. Tersoff and Hamann presented this more realistic model in the 1980s [9, 10]. Their starting point was a first-order perturbation theory model introduced by Bardeen [11]. In this model the tunneling is described by the tunneling matrix $M_{\mu,\nu}$, which represents the overlap of the wave functions of tip Ψ_μ and surface Ψ_ν .

The tunneling current for a general geometry can then be written as:

$$I = \frac{2\pi e}{\hbar} \sum_{\mu, \nu} f(E_\mu) [1 - f(E_\nu + eV)] |M_{\mu, \nu}|^2 \delta(E_\mu - E_\nu) \quad (2.5)$$

Where $f(E)$ is the Fermi-Dirac distribution function and E_μ and E_ν the energies of the states of surface and tip. V is the applied bias voltage. In the limit of low temperature and voltages $e \cdot V \ll \Phi$, Eq. 2.5 can be simplified because $f(E)$ becomes a step function with $f(E) = 1$ for $E < E_F$. We can thus approximate the term $[1 - f(E_\nu + eV)]$ as a step function, which yields:

$$I = \frac{2\pi}{\hbar} e^2 V \sum_{\mu, \nu} |M_{\mu, \nu}|^2 \delta(E_\mu - E_F) \delta(E_\nu - E_F) \quad (2.6)$$

The tunneling matrix element $M_{\mu, \nu}$, was shown by Bardeen [11] to be Eq. 2.7 integrated over an arbitrary surface between tip and surface:

$$M_{\mu, \nu} = -\frac{\hbar^2}{2m} \int \left(\Psi_\mu^* \vec{\nabla} \Psi_\nu - \Psi_\nu \vec{\nabla} \Psi_\mu^* \right) d\vec{S} \quad (2.7)$$

In order to arrive at quantitative tunneling currents it is necessary to define the wave functions for surface and tip. These should describe the geometry found in an STM. The surface is described through a wave function parallel to the surface, consistent with Bloch's theorem. In the perpendicular direction it decays exponentially into the vacuum:

$$\Psi_\nu = V_{\text{surface}}^{-1/2} \sum_G a_G \underbrace{e^{\left(-\sqrt{\kappa^2 + |\vec{k}_\parallel + \vec{G}|^2} z\right)}}_{\text{Exp.decay}} \cdot \underbrace{e^{i[\vec{k}_\parallel + \vec{G}] \vec{x}}}_{\text{Blochwave}} \quad (2.8)$$

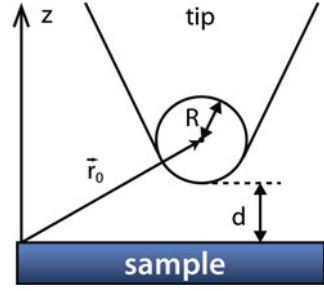
where \vec{G} is a reciprocal lattice vector, $\kappa = \hbar^{-1}(2m\Phi)$ the decay length into the vacuum, \vec{k}_\parallel the wave vector of the surface wave, and V_{surface} the normalization volume of the surface. The first few coefficients a_G are typically of order unity. The tip is modeled as a spherical potential (see Fig. 2.4) at the point closest to the surface and the rest is arbitrary. Accordingly the spherical s-wave function is used for the tip:

$$\Psi_\mu = V_{\text{tip}}^{-1/2} \kappa R e^{\kappa R} \frac{1}{\kappa |\vec{r} - \vec{r}_0|} e^{-\kappa |\vec{r} - \vec{r}_0|} \quad (2.9)$$

here V_{tip} is the normalization volume of the tip, R the tip radius, κ and Φ are the same constants as mentioned above. For simplicity's sake the work function of both tip and surface are assumed to be equal. With these model wave functions, it is possible to simplify the tunneling matrix (Eq. 2.7) to:

$$M_{\mu, \nu} = \frac{\hbar^2}{2m} 4\pi k^{-1} V_{\text{tip}}^{-1/2} \kappa R e^{\kappa R} \Psi_\nu(\vec{r}_0) \quad (2.10)$$

Fig. 2.4 Model used to approximate the wave function of the tip in the Tersoff Hamann description. The center of the tip is at \vec{r}_0 with an assumed spherical geometry, R is the radius and d the distance to the surface



Finally, Eq. 2.10 can be used to define the tunneling current (Eq. 2.6) giving:

$$I = 32 \frac{\pi^3}{\hbar k^4} e^2 V \Phi^2 R^2 e^{2kR} \frac{1}{V_{\text{tip}}} \sum_{\mu\nu} |\Psi_\nu(\vec{r}_0)|^2 \delta(E_\mu - E_F) \delta(E_\nu - E_F) \quad (2.11)$$

To simplify this expression we note that the local density of states for tip and surface are defined as follows:

$$\rho_{\text{tip}}(E) = \frac{1}{V_{\text{tip}}} \sum_{\mu} \delta(E_\mu - E) \quad (2.12)$$

$$\rho_{\text{surface}}(E, \vec{r}_0) = \sum_{\nu} |\Psi_\nu(\vec{r}_0)|^2 \delta(E_\nu - E) \quad (2.13)$$

The final expression for the tunneling current comes to:

$$I \propto V \rho_{\text{tip}}(E_F) \rho_{\text{surface}}(E_F, \vec{r}_0) \quad (2.14)$$

Thus the current depends on the local density of states (LDOS) of the surface at the position of the tip \vec{r}_0 at the Fermi-Energy E_F . This means that STM images the LDOS of the surface rather than the position of atoms.

A more realistic description, a generalization of the Tersoff-Hamann model, defines the tunneling current by integrating over the states contributing to the tunneling current: the surface and tip DOS within the finite bias window. The dependence of the vacuum barrier on the tip-sample distance d , the energy E of each state, and the bias voltage V are represented by a transmission coefficient $T(d, E, eV)$ [12–14].

$$I \propto \int_{E_F}^{E_F + eV} \rho_{\text{surface}}(E_F - eV + \varepsilon) \rho_{\text{tip}}(E_F + \varepsilon) T(d, \varepsilon, eV) d\varepsilon \quad (2.15)$$

We have thus found the contributing factors to the tunneling current: The DOS of tip and sample, and a transmission coefficient $T(d, E, eV)$. For small biases

ρ_{tip} and T can be assumed constant; the tunneling current would then be primarily proportional to ρ_{surface} integrated from E_F to the applied bias voltage $E_F + V$.

This model is still not a complete description of the tunneling process in an STM. Although in many standard situations it provides a reasonable qualitative picture. Some critical remarks have to be added nonetheless. The approximation of the tip as an s orbital is rather inaccurate, as in tungsten tips the d orbitals contribute to the major part of the tunneling current [15]. Also, the interaction between tip and sample through microscopic chemical forces is not always negligible.

2.2 Scanning Tunneling Spectroscopy

2.2.1 Elastic Tunneling Spectroscopy

One of the key features of an STM setup is the ability to measure the electronic structure of a sample at the position of the tip. The basic principles of the scanning tunneling spectroscopy (STS) mode can be understood from Eq. 2.15. If the transmission coefficient T and to some extent ρ_{tip} are assumed to be constant for the given energy interval, we can approximate the differential conductance dI/dV as:

$$\frac{dI}{dV} \propto \rho_{\text{surface}}(E_F - eV) \cdot \rho_{\text{tip}}(E_F) \quad (2.16)$$

The differential conductance dI/dV is hence directly proportional to the local density of states of the sample at the position of the tip. Depending on the sign of applied bias the occupied or the unoccupied states are measured (see Fig. 2.5).

In STM experiments the STS signal is obtained by positioning the tip over the point of interest, then the tunneling gap is set to an appropriate setpoint, the feedback loop is opened to allow the current to vary and the voltage is ramped to cover the region of interest. The voltage setpoint should be set value that integrates the same DOS in all points investigated on the sample, to avoid strong variations in the tip height. This is, however, a complex task in inhomogeneous systems such as molecular adsorbates on surfaces, and not always possible due to limitations in the measurement apparatus. Hence, usually, while not entirely correct, the starting voltage of the voltage ramp was used in this work.

2.2.2 Inelastic Tunneling Spectroscopy

In addition to the elastic tunneling, electrons can couple to internal degrees of freedom during the tunneling process. Examples of these are molecular vibrations [7], and spin excitations [16]. In the case of tunneling to/from a molecule, inelastic processes

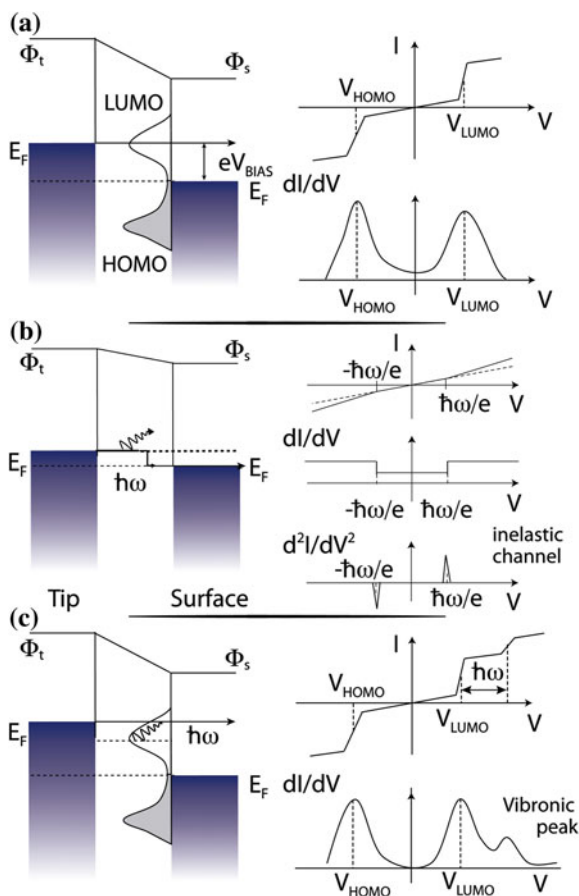


Fig. 2.5 Schematics of STS through a molecule. Energy level diagrams showing elastic and inelastic processes, occurring at positive biases. Φ_t and Φ_s are the work functions of tip and sample, respectively. **a** Elastic tunneling: electrons tunnel from the tip into the sample probing the unoccupied states around E_F of the sample. The dI/dV curve shows a peak at the position of a molecular orbital. **b** Inelastic tunneling. Electrons excite a vibration in the molecule and lose energy. The opening of this inelastic channel increases the conductance at the energy of the vibration. This is resolved as symmetric steps in the dI/dV curve and antisymmetric peaks at opposite polarities in the d^2I/dV^2 spectrum. **c** Tunneling process with vibronic excitation at a molecular orbital. The vibronic peak is represented as extra protrusions in the dI/dV spectra at energy separations of the excited phonon

can be excited, depending on the cross-section between molecular orbital and the excitation, the orientation of the molecule, the position of the tip, etc. Once an electron has the required energy to excite the process, the interaction leads to the opening of another tunneling channel. Such processes lead to a change in the slope of the I/V curve, that is, to a symmetric step function in the dI/dV and antisymmetric peaks in the d^2I/dV^2 (Fig. 2.5b). By recording the d^2I/dV^2 curve these excitations can be

effectively measured. Resonant tunneling through electronic states can also couple to inelastic processes. If the lifetime of a given electronic state is long enough, such as in the case of decoupled molecular orbitals, an electron tunneling to this state can couple to vibrations. These so-called vibronic excitations are then detected as extra satellite peaks in the dI/dV signal at multiples of the energy of the vibrational mode above the molecular resonances (Fig. 2.5c).

2.2.3 Lock-in Technique

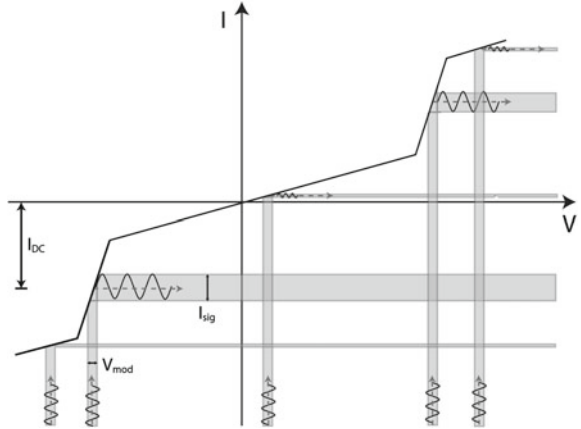
In an experimental setup the dI/dV signal can be recorded directly using a lock-in amplifier. Compared to a numerical calculation from the I/V curve, this method yields a better dynamic range and signal to noise ratio.

A small sinusoidal voltage modulation ($V_{mod} = v_o \sin(\omega_r t)$, with $v_o = 0.1$ to 100 mV) is added to the bias voltage, causing a sinusoidal response in the tunneling current. The amplitude of the modulated current is sensitive to the slope of the I-V curve (see Fig. 2.6). The resulting current signal is then converted by the preamplifier to a voltage:

$$V_{in} = V_{sig}^I \sin(\omega_r t + \theta_{sig}) + V_{DC}^I + V_{noise}^I(t) \quad (2.17)$$

where V_{DC}^I is the DC part of the current, and V_{noise}^I the noise present in the system θ_{sig} is the phase of the measurement signal. The lock-in then multiplies this signal with a sinus wave $V_{ref} = V_l \sin(\omega_r t + \theta_l)$, resulting in an output of:

Fig. 2.6 The origin of the derivative in a lock-in measurement. During an I-V ramp for STS a sinusoidal signal is added to the bias voltage. The resulting modulation in the tunneling current has an amplitude proportional to the slope of the I-V curve, hence a dI/dV signal



$$V_{psd} = V_{sig} V_l \sin(\omega_r t + \theta_{sig}) \sin(\omega_l t + \theta_l) + V_{ref}(t) V_{DC} + V_{ref}(t) V_{noise}(t) \quad (2.18)$$

$$= 1/2 V_{sig} V_{ref} \cos([\omega_r - \omega_r]t + \theta_{sig} - \theta_l) - 1/2 V_{sig} V_{ref} \cos([\omega_r + \omega_r]t + \theta_{sig} + \theta_l) + V_{ref}(t) V_{DC} + V_{ref}(t) V_{noise}(t) \quad (2.19)$$

The signal is then passed through a low pass filter, which is done integrating the signal over a given time τ . A higher integrating time means a lower pass bandwidth, resulting in a better signal-to-noise ratio. The time dependent terms will be removed by this operation, leaving only the first term of Eq. 2.19:

$$V_{psd} = 1/2 V_{sig} V_l \cos(\theta_{sig} - \theta_{ref}) \quad (2.20)$$

and only the Fourier components of the noise term with frequencies close to the reference ω_r . This way any noise present in the signal will be strongly reduced by the band pass filter. To minimize the Fourier components of the noise passing the filter, frequencies which do not interfere with the internal resonances (mechanical or electrical) of the experimental setup and are within the bandwidth of the current amplifier are used ($\omega_r = 0.5 - 3$ kHz).

The lock-in electronics assure that the phase relation ($\theta_{sig} - \theta_{ref}$) between the lock-in modulation and the measurement signal is time-independent. Its value should be chosen so that the detected signal becomes maximum $\cos(\theta) = 1$.

Higher derivatives can also be measured using higher harmonics of the signal [17]. The second harmonic will be used to perform inelastic spectroscopy via the d^2I/dV^2 signal.

The dI/dV signal measured in units of conductance [$nS = nA/V/V$]. The conversion between the lock-in output and conductance units follows directly:

$$\frac{dI}{dV} = \left(\text{signal} \cdot \frac{\text{lock-in sensitivity}}{\text{lock-in full scale}} \cdot \text{preamplifier gain} \right) \cdot \frac{1}{\text{lock-in modulation}}$$

2.2.4 Background Subtraction

The dI/dV signal is convoluted with the DOS of the tip, which in real experiments is *not* constant. Therefore great care has to be taken to prepare the tip, not only to be sharp in order to achieve good topography resolution, but also to obtain a featureless DOS. However, the shape and DOS of the tip can only be manipulated in very indirect ways. A wide range of methods have been developed, e.g. by voltage pulses, or small controlled contacts with the surface, but non of them is very reproducible and they all

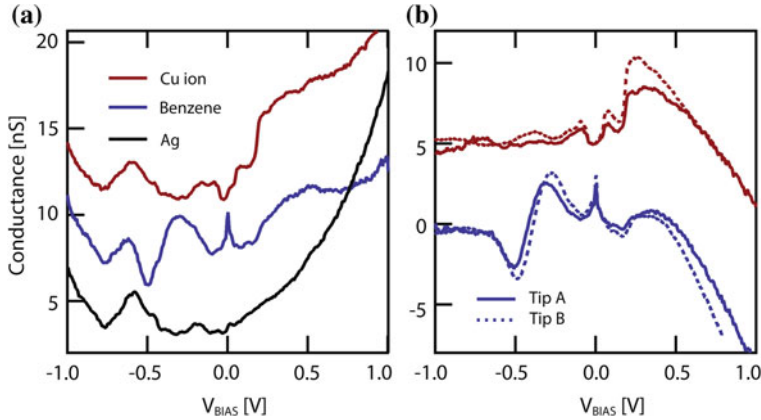


Fig. 2.7 **a** dI/dV spectra acquired on the Cu ion (red), and benzene (blue) of a single CuPc molecule on a Ag(100) surface, and on a clean spot of the Ag (black) with tip A (3.0 nA, -1.0 V). The spectra have been y-offset for clarity, all of them start at ~ 10 nS, like the blue spectra. **b** The same ion and benzene spectra after subtraction of the Ag spectrum (solid lines). For comparison, we show a pair of background subtracted spectra (dotted lines) acquired with a different tip (B) and initial setpoint (3.0 nA, -2.0 V). The intensity of the latter have been reduced by a factor of 2 to account for the different initial setpoint. The spectra recorded on the Cu ion have been vertically shifted by 5 nS for better visibility

are time intensive. The results will vary from tip to tip, and the tip may even change in between STS measurements.

A very efficient method to reduce the impact of tip DOS features is background subtraction. The basic idea is to measure the LDOS of the tip and the surface on a clean spot of the sample surface using the same feedback conditions as for the sample's feature of interest. This data can then be used to deconvolute effects on the STS taken on the point of interest. Theoretically a mathematical deconvolution operation would be required to remove tip and surface contribution of the STS. However, as P.Wahl et al. pointed out [18], a subtraction of the two STS curves is often sufficient, and leads to good results if the tip reference spectra does not present any sharp features. Figure 2.7 shows an example of background subtraction of dI/dV spectra recorded on CuPc/Ag(100). It can be observed that after subtraction the spectra taken with different tips are essentially the same. Furthermore, the tip related feature appearing around -0.6 V in the raw spectrum is removed, showing the efficacy of this method. Throughout this work all background subtracted spectra are obtained in this manner.

Nonetheless there are certain artifacts that can be created by this method, i.e., strong tip features can lead to artificial peaks in the resulting curves. Furthermore the conductance values reported for the spectra represent relative values. Negative dI/dV values mean that the conductance at the point of interest at a certain energy is lower than that of the substrate (see Fig. 2.7b).

2.2.5 Differential Conductance Maps

An intriguing application of STM lies in the possibility to spatially resolve the topography of subnanoscale systems. The technique can be combined with STS, mapping the spatial distribution of features found in STS. The basic method is to scan an area of interest and take the dI/dV intensity at each point of the scan. The resulting dI/dV map is to some extent an image of the spatial distribution of the state investigated. The speed of such an acquisition is limited by the τ setting of the lock-in amplifier (5–8 τ per point) and the pixel resolution of the dI/dV map. Depending on its size the measurement time in our experiments varied between 5–30 min, meaning that the effect of thermal drift becomes important. To counteract the thermal drift in the z direction the constant current mode is usually employed.¹

The interpretation of such dI/dV maps is however not straightforward, because the topography of the sample has a strong influence on the height of the tip and will enhance or reduce certain spectral features. A variety of normalization techniques for dI/dV spectra and maps exist, and provide useful results in particular situations [14, 19–22]. In any case, the qualitative comparison of molecular states for similar molecules in different environments, as presented in later chapters, is not severely affected by topographic effects, therefore in this work no normalization techniques were used.

2.3 Manipulation Techniques

Another powerful feature of STM at low temperature is the possibility to locally manipulate the investigated system, by moving atoms or molecules with the tip. This is a great tool for scientific research as it allows control of the positions of single atoms and molecules to create new nanosystems and investigate them. The manipulation process is controlled through three main parameters in the STM: the electric field, the tunneling current, and the short range interactions between tip and surface [6, 23]. Care has to be taken to find for each specific system the right combination of parameters. There are two main methods employed for manipulation: vertical and lateral manipulation (see Fig. 2.8).

In the vertical manipulation mode, field and current effects play a major role. Here the tip is also approached towards the adsorbate while a voltage pulse is applied. With the correct parameters this transfers the adsorbate to the tip, which is effectively “picked up”. Afterwards the tip is retracted and moved to a new location where a reverse pulse and approach drops the adsorbate again. In a related application this method can be used to modify the tip, to gain access to different spectral features due to changes of the symmetry of tunneling orbitals [24].

In the lateral manipulation mode, the tip is approached towards the surface, on top of the atom/molecule that has to be moved, by increasing the current and lowering

¹ However with carefully chosen parameters a constant height map is also possible.

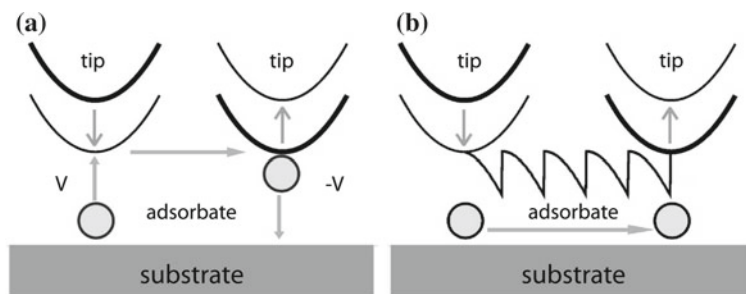


Fig. 2.8 **a** Sketch of the vertical manipulation procedure: 1. The tip is placed above the molecule/atom 2. To transfer an adsorbate to the tip a voltage pulse is applied while moving the tip towards the atom 3. The tip is retracted and moved to the desired position 4. The reverse pulse from the pick up is applied to drop the adsorbate. **b** The lateral manipulation process in constant current mode: 1. The tip is placed above the molecule/atom 2. The tip is approached towards the atom by increasing the current and decreasing the bias voltage 3. The tip is moved along the desired pathway. The tip height curve shows the movement of the adsorbate on the surface. Images adapted from [6]

the bias voltage (e.g. for Li on Ag(100) the conditions were 50 mV, 250 nA). Then the tip follows the desired pathway and finally is retracted again. If the interaction between tip and atom, such as vdW, chemical forces or the electric field, is strong enough the atom is moved along with the tip. The molecules can either be pushed or pulled depending on the specific system, leading to characteristic tip height curves. A pulling movement, consists of a step increase as the molecule is pulled under the tip, and subsequent slow decrease as the tip moves away from it (see Fig. 2.9a). For a pushing manipulation the curve would be mirrored, starting with a slow rise, followed by a sharp drop as the molecule jumps forward.

Both types of manipulation were used for the first time by the group of Don Eigler at IBM-Almaden [25] and later in Berlin [26] to build nanostructures from single atoms and molecules. Throughout this work mainly the lateral manipulation mode has been used to move atoms and molecules. In Fig. 2.9 the creation of a 3x3 cluster of CuPc molecules is shown.

2.4 Experimental Setup

The experimental setup used in this work is a low temperature STM based on a design by G. Meyer [27], and commercially available from Createc Fischer and Co GmbH Berlin, Germany [28]. The system operates in an ultra high vacuum (UHV) environment ($p < 2 \times 10^{-10}$ mBar), and is based on a liquid helium cryostat to work at temperatures ~ 5 K. In this section a brief review of the capabilities and limitations of this STM will be presented.

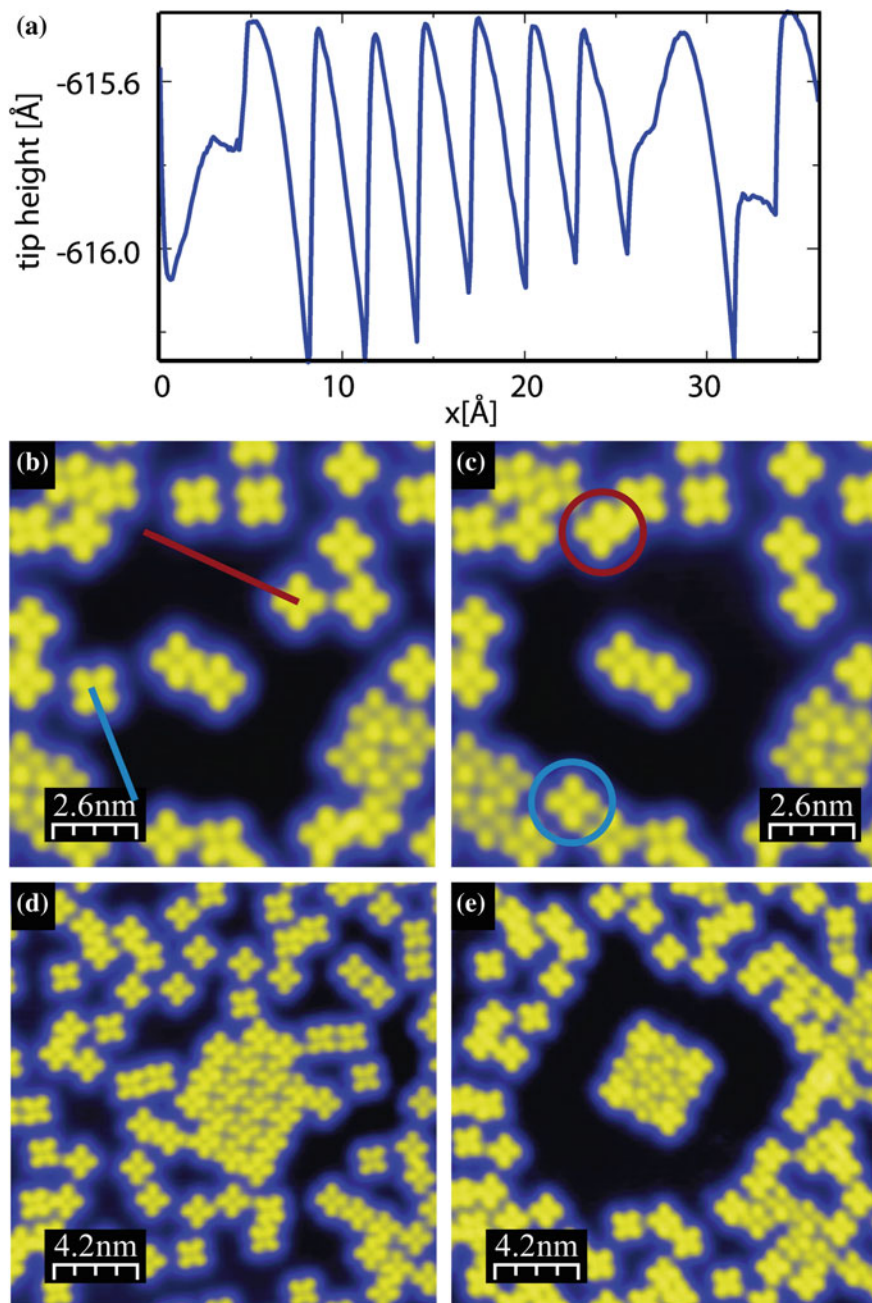


Fig. 2.9 **a** Tip height signal during the lateral manipulation of a CuPc adsorbed on Ag(100), corresponding to a pulling movement **b** and **c** STM topography before and after dragging two CuPc molecules. A gap resistance of $333 \text{ K}\Omega$ ($1.5 \times 10^5 \text{ nA}$, 50 mV) was used for manipulation, and $1000 \text{ M}\Omega$ (0.1 nA , 100 mV) for imaging. **d** and **e** Images before and after the formation of a 3×3 square cluster (see Sect. 5.4.1)

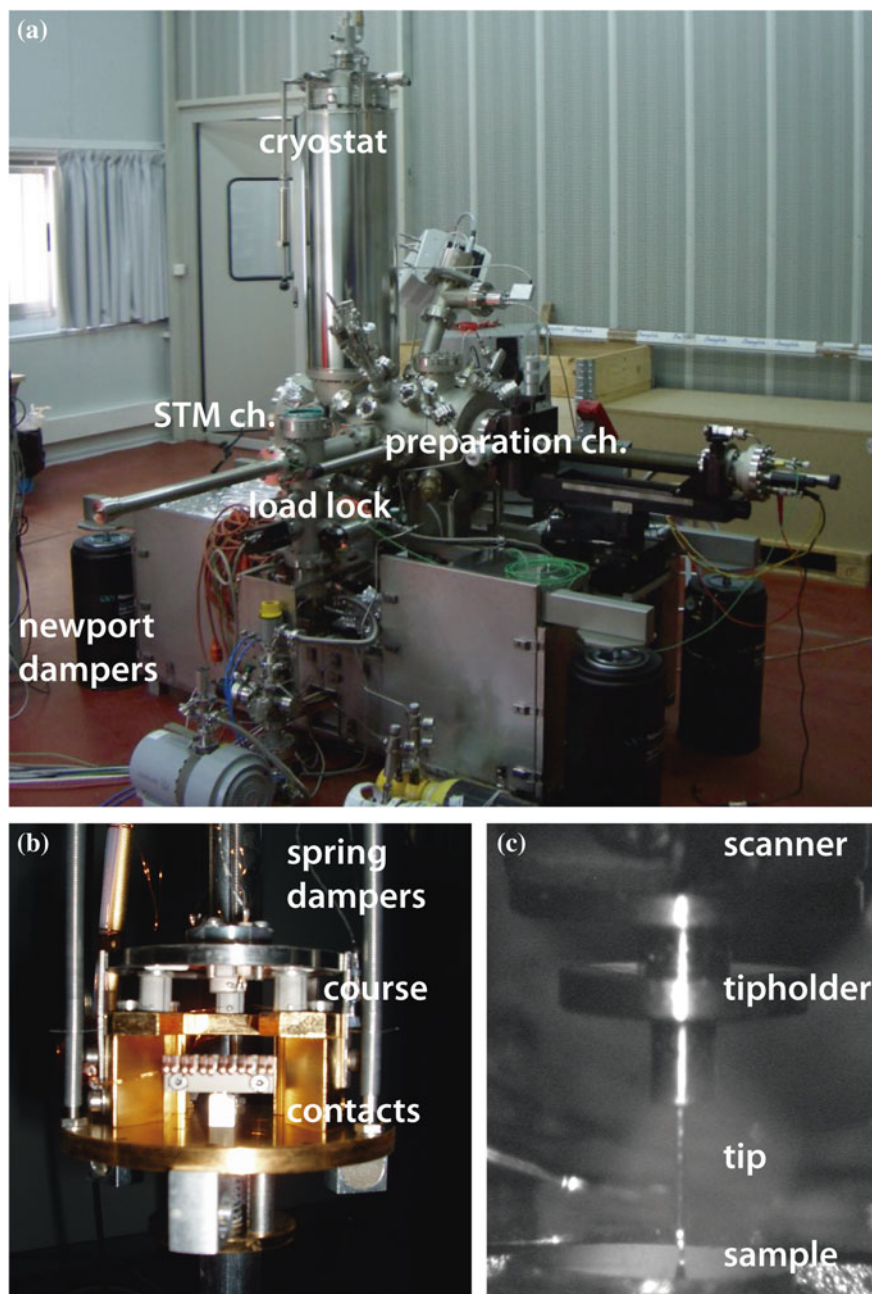


Fig. 2.10 **a** The low temperature STM vacuum chamber: The STM is located below the cryostat, the preparation chamber features a sputter gun for cleaning the samples, a LEED optic, and several evaporators: The quadruple OMBE for molecular sources, a triple Omicron for metals. The STM chamber has an in-situ Alkali evaporator and a single metal evaporator. **b** The low temperature STM head and the sample stage is shown: The sample holder is placed between the coarse motion ramp and the contacts. The whole setup is hanging on three springs to decouple it from external vibrations. **c** The piezo scanner and the tip in a tunneling position

Figure 2.10 shows the vacuum chamber of the STM: It consists of two chambers, one used for sample preparation and a second that houses the STM and its cryostat. The UHV is generated by an array of pumps: Two ion pumps one in each chamber, a turbo-molecular pump and a titanium sublimation pump on the preparation chamber. The cryostat itself also acts as cryo-pump in the STM chamber.

The Cooling System

The low operation temperatures are achieved by the use of a bath cryostat, made of two tanks. The inner one holds up to 11 litres of liquid helium while the outer one is filled with liquid nitrogen. Both cooling stages have aluminum radiation shields that enclose the STM sample stage within. Using this method the sample can be kept cool and measured for up to 100 h per refill of the helium deposit. The nitrogen tank lasts for approximately 48 h.

STM Head

The core of the STM setup is the STM head, shown in Fig. 2.10b. It hangs from the bottom of the He tank on three springs, which together with an Eddy current damping system decouple it from external vibrations. The STM head uses a Besocke type ramp to approach the tip to the sample until a tunneling current is detectable. The Besocke system is based on a plate that has three low angled ramps on its bottom side. This plate lies on three piezo tube actuators, which can displace the plate in x-y direction or rotate it, using a slip stick motion. Due to the ramps in the plate a rotation results in a z movement approaching or retracting the tip to/from the sample (maximum range 300 μm). The x-y movements of the ramp allow access to a large part of the sample surface for scanning. A fourth piezo tube actuator attached to the center of the ramp is the actual piezo scanner, which performs the x-y-z position during the STM measurements. The tip is placed in an in-situ exchangeable tip holder, which is attached to the piezo tube by a small magnet (see Fig. 2.10c).

Sample Preparation Facilities

The system is equipped with a sputter gun in the preparation chamber. To obtain atomically clean metal surfaces, the samples are bombarded with Ar^+ ion, which removes impurities and adsorbates. The increased surface roughness is then smoothed by annealing the sample with an oven that is mounted on the sample holder. This process has to be repeated a number of times to obtain a good sample surface. The overall quality of the surface can be checked with a LEED setup, before and after deposition of molecules/atoms etc. on the surface. Several evaporator slots are present and a wide range of samples can be prepared: A commercial triple e-beam metal evaporator can be used to grow thin metal films, a quadruple Kundsén cell

evaporator deposits molecules, and several single evaporators for molecules and metals are available. The main manipulator of the chamber can be cooled with liquid nitrogen, so that the sample temperature during deposition can be chosen between $-180\text{ }^{\circ}\text{C}$ to $800\text{ }^{\circ}\text{C}$. It is further possible to deposit materials in-situ on the sample, by a small door in the cooling shields of the STM. This slot is also equipped with a fixed home-built alkali evaporator, working with cells from SAES getters.

2.5 Methods

Sample Preparation

In order to investigate MePc (Me = Fe, Co, Ni, Cu) molecules adsorbed on the Ag(100) substrate, we prepared several samples of varying molecular coverages. To avoid contamination all experiments were undertaken under ultra high vacuum (UHV) conditions ($p < 2 \times 10^{-10}$ mbar). Before the MePc (Sigma Aldrich, 99% pure powder) they can be used in UHV, it is necessary to thoroughly degas the powder to achieve a base pressure during evaporation below $p < 5 \times 10^{-10}$ mbar.

First we cleaned the Ag(100) (Surface Preparation Laboratories) surface by repeated sputtering with Ag^+ ions and subsequent annealing to 450°C . We monitored the surface quality by Low Energy Electron Diffraction (LEED). Once a clean surface was obtained the molecules were evaporated from the molecular beam source onto the sample, which was kept at room temperature. The Knudsen cell of the evaporator was heated to 440°C ,² which yielded a deposition rate of approximately 0.05 molecular layers per minute. In this way samples of different MePc coverages could be produced, which were then transferred into the STM sample stage. All measurements were carried out at 5 K in order to inhibit molecular mobility and perform single molecule spectroscopy and manipulation.

The doping experiments were prepared by in-situ deposition of Li or Fe atoms, as a second step after a MePc preparation. The source for the Li was a well degassed Li dispenser (SAES) heated by direct current flow (6 A). For the Fe atoms an electron beam evaporator was used.

STS Settings

The dI/dV spectra were obtained using the lock-in technique, using a bias voltage modulation of frequency around 3 kHz and amplitude 1 mV_{rms} for the low range spectra, 3 mV_{rms} for the larger energy range and 10 mV for dI/dV maps. Since zero bias resonances cannot be measured with closed feedback, we have mapped the conductance near E_F by measuring the second derivative of the current, mapping the maximum of the d^2I/dV^2 signal, which is slightly offset from $V_b = 0$, as shown in

² This temperature is measured on the outside of the crucible close to the filament and therefore does not represent be the actual temperature of the molecules during the deposition.

Fig. 2.11 Comparison between first (black) and second derivative (blue) of a CuPc spectrum showing a Kondo resonance. The maximum of the second derivative at negative voltage is used to map the Kondo resonance

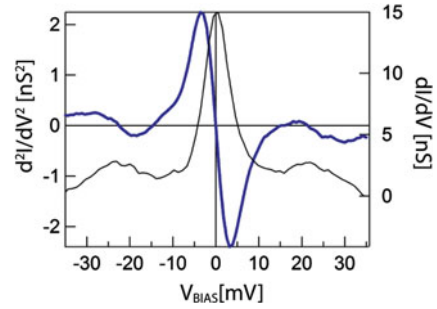


Fig. 2.11. The validity of this approach is justified by the fact that, for a Lorentzian function, the intensity maximum of the peak is proportional to the (shifted) maximum of its derivative.

Density Functional Theory Methods

The spectroscopic results have been compared to the electronic structure obtained from ab-initio calculations performed by R. Robles, N. Lorente, R. Korytár, and P. Ordejón, using the VASP implementation of Density Functional Calculations (DFT) in the projected augmented plane wave scheme [29, 30]. Different approximations, each with different limitations and over- or underestimations have been compared in order to obtain consistent results, and to check the effect of different exchange-correlation approximations or the van der Waals (vdW) interaction. Namely the Local Density Approximation (LDA) [31], Generalized Gradient Approximation (GGA) [32], GGA+vdW [33, 34], the DSRL functional, designed to include VdW [35–38], and LDA+U [39] were used. The plane wave cutoff energy was set to 300 eV. The calculated slab included 5 Ag atomic layers intercalated by 7 vacuum layers in the vertical direction, and a 7×7 lateral supercell. The positions of all atoms in the molecule and the first three Ag layers were relaxed vertically and laterally until forces were smaller than 0.05 eV/Å. The Projected Density of States (PDOS) of NiPc has been used to compare single ($1 \times 1 \times 1$) and multiple ($5 \times 5 \times 1$) k point calculations, which converge after applying a broadening of 100 meV to the data. Based on that, the results for a single k point with the latter broadening are used in the following. Charge transfer and local magnetic moments have been calculated using a Bader charge analysis [40, 41].

References

1. H. Binnig, G. Rohrer. Scanning tunnelling microscopy. *Helv. Phys. Acta.* **55**(6), 726–735 (1982)
2. G. Binnig, H. Rohrer, C. Gerber, E. Weibel, Tunneling through a controllable vacuum gap. *Appl. Phys. Lett.* **40**(2), 178–180 (1982)

3. G. Binnig, H. Rohrer, C. Gerber, E. Weibel. Surface studies by scanning tunneling microscopy. *Phys. Rev. Lett.* **49**(1), 57 (1982)
4. G. Binnig, K.H. Frank, H. Fuchs, N. Garcia, B. Reihl, H. Rohrer, F. Salvan, A.R. Williams. Tunneling spectroscopy and inverse photoemission: image and field states. *Phys. Rev. Lett.* **55**(9), 991 (1985)
5. H.C. Manoharan, C.P. Lutz, D.M. Eigler. Quantum mirages formed by coherent projection of electronic structure. *Nature* **403**(6769), 512–515 (2000). doi:[10.1038/35000508](https://doi.org/10.1038/35000508)
6. F. Moresco. Manipulation of large molecules by low-temperature STM: model systems for molecular electronics. *Phys. Rep.* **399**(4), 175–225 (2004). doi:[16/j.physrep.2004.08.001](https://doi.org/10.1016/j.physrep.2004.08.001)
7. W. Ho. Single-molecule chemistry. *J. Chem. Phys.* **117**, 11033 (2002). doi:[10.1063/1.1521153](https://doi.org/10.1063/1.1521153)
8. C. Cohen-Tannoudji. *Quantenmechanik 1*. (Walter de Gruyter, Berlin, 1999), p. 64ff
9. J. Tersoff, D.R. Hamann. Theory and application for the scanning tunneling microscope. *Phys. Rev. Lett.* **50**(25), 1998 (1983)
10. J. Tersoff, D.R. Hamann. Theory of the scanning tunneling microscope. *Phys. Rev. B* **31**(2), 805 (1985)
11. J. Bardeen. Tunnelling from a many-particle point of view. *Phys. Rev. Lett.* **6**(2), 57 (1961)
12. N.D. Lang. Spectroscopy of single atoms in the scanning tunneling microscope. *Phys. Rev. B* **34**(8), 5947–5950 (1986). doi:[10.1103/PhysRevB.34.5947](https://doi.org/10.1103/PhysRevB.34.5947)
13. A. Selloni, P. Carnevali, E. Tosatti, C.D. Chen. Voltage-dependent scanning-tunneling microscopy of a crystal surface: graphite. *Phys. Rev. B* **31**(4), 2602–2605 (1985). doi:[10.1103/PhysRevB.31.2602](https://doi.org/10.1103/PhysRevB.31.2602)
14. V.A. Ukraintsev. Data evaluation technique for electron-tunneling spectroscopy. *Phys. Rev. B* **53**(16), 11176–11185 (1996). doi:[10.1103/PhysRevB.53.11176](https://doi.org/10.1103/PhysRevB.53.11176)
15. J. Buisset. *Tiefteperatur Rastertunnelmikroskopie* (Wissenschaft und Technik Verlag, Berlin, 1996)
16. A.J. Heinrich. Single-atom spin-flip spectroscopy. *Science* **306**(5695), 466–469 (2004). doi:[10.1126/science.1101077](https://doi.org/10.1126/science.1101077)
17. Stanford Research Systems. Model SR810 DSP Lock-In amplifier—manual, January 2005. URL <http://www.thinksrs.com/mult/SR810830m.htm>
18. P. Wahl, L. Diekhoner, M.A. Schneider, K. Kern. Background removal in scanning tunneling spectroscopy of single atoms and molecules on metal surfaces. *Rev. Sci. Instrum.* **79**(4), 043104–043104-4 (2008). doi:[10.1063/1.2907533](https://doi.org/10.1063/1.2907533)
19. J.A. Stroscio. Imaging electronic surface states in real space on the Si(111) 2×1 surface. *J. Vac. Sci. Technol., A: Vacuum, Surfaces, and Films* **5**, 838 (1987). doi:[10.1116/1.574321](https://doi.org/10.1116/1.574321)
20. J. Li, W. Schneider, R. Berndt. Local density of states from spectroscopic scanning-tunneling-microscope images: Ag(111). *Phys. Rev. B* **56**(12), 7656–7659 (1997). doi:[10.1103/PhysRevB.56.7656](https://doi.org/10.1103/PhysRevB.56.7656)
21. Y. Yayon, X. Lu, M.F. Crommie. Bimodal electronic structure of isolated Co atoms on Pt(111). *Phys. Rev. B* **73**(15), 155401 (2006). doi:[10.1103/PhysRevB.73.155401](https://doi.org/10.1103/PhysRevB.73.155401)
22. M. Ziegler, N. Néel, A. Sperl, J. Kröger, R. Berndt. Local density of states from constant-current tunneling spectra. *Phys. Rev. B* **80**(12), 125402 (2009). doi:[10.1103/PhysRevB.80.125402](https://doi.org/10.1103/PhysRevB.80.125402)
23. P. Avouris. Manipulation of matter at the atomic and molecular levels. *Acc. Chem. Res.* **28**(3), 95–102 (1995). doi:[10.1021/ar00051a002](https://doi.org/10.1021/ar00051a002)
24. L. Gross, N. Moll, F. Mohn, A. Curioni, G. Meyer, F. Hanke, M. Persson. High-resolution molecular orbital imaging using a p-wave STM tip. *Phys. Rev. Lett.* **107**(8), 086101 (2011). doi:[10.1103/PhysRevLett.107.086101](https://doi.org/10.1103/PhysRevLett.107.086101)
25. J.A. Stroscio, D.M. Eigler. Atomic and molecular manipulation with the scanning tunneling microscope. *Science* **254**(5036), 1319–1326 (1991). doi:[10.1126/science.254.5036.1319](https://doi.org/10.1126/science.254.5036.1319)
26. G. Meyer, K. Rieder. Controlled manipulation of single atoms and small molecules with the scanning tunneling microscope. *Surf. Sci.* **377–379**(0), 1087–1093 (1997). doi:[10.1016/S0039-6028\(96\)01551-8](https://doi.org/10.1016/S0039-6028(96)01551-8)
27. G. Meyer. A simple low-temperature ultrahigh-vacuum scanning tunneling microscope capable of atomic manipulation. *Rev. Sci. Instrum.* **67**(8), 2960 (1996). doi:[10.1063/1.1147080](https://doi.org/10.1063/1.1147080)

28. CreaTec Fischer and Co. GmbH. “STM/AFM systems”,. <http://www.createc.de/products/lt-stm-afm-systems.html>. URL <http://www.createc.de/products/lt-stm-afm-systems.html>
29. G. Kresse and J. Furthmüller. Efficiency of ab-initio total energy calculations for metals and semiconductors using a plane-wave basis set. *Comput. Mater. Sci.* **6**(1), 15–50 (1996). doi:[10.1016/0927-0256\(96\)00008--0](https://doi.org/10.1016/0927-0256(96)00008--0)
30. G. Kresse, D. Joubert, From ultrasoft pseudopotentials to the projector augmented-wave method. *Phys. Rev. B* **59**(3), 1758 (1999)
31. J.P. Perdew, A. Zunger. Self-interaction correction to density-functional approximations for many-electron systems. *Phys. Rev. B* **23**(10), 5048 (1981). doi:[10.1103/PhysRevB.23.5048](https://doi.org/10.1103/PhysRevB.23.5048)
32. J.P. Perdew, K. Burke, M. Ernzerhof. Generalized gradient approximation made simple. *Phys. Rev. Lett.* **77**(18), 3865–3868 (1996). doi:[10.1103/PhysRevLett.77.3865](https://doi.org/10.1103/PhysRevLett.77.3865)
33. S. Grimme. Semiempirical GGA-type density functional constructed with a long-range dispersion correction. *J. Comput. Chem.* **27**(15), 1787–1799 (2006). doi:[10.1002/jcc.20495](https://doi.org/10.1002/jcc.20495)
34. T. Bučko, J. Hafner, S. Lebègue, J.G. Ángyán. Improved description of the structure of molecular and layered crystals: Ab initio DFT calculations with van der waals corrections. *J. Phys. Chem. A* **114**(43), 11814–11824 (2010). doi:[10.1021/jp106469x](https://doi.org/10.1021/jp106469x)
35. M. Dion, H. Rydberg, E. Schröder, D.C. Langreth, B.I. Lundqvist. Van der waals density functional for general geometries. *Phys. Rev. Lett.* **92**(24), 246401 (2004). doi:[10.1103/PhysRevLett.92.246401](https://doi.org/10.1103/PhysRevLett.92.246401)
36. D.C. Langreth, B.I. Lundqvist, S.D. Chakarova-Käck, V.R. Cooper, M. Dion, P. Hyldgaard, A. Kelkkanen, J. Kleis, L. Kong, S. Li, P.G. Moses, E. Murray, A. Puzder, H. Rydberg, E. Schröder, T. Thonhauser. A density functional for sparse matter. *J. Phys.: Condens. Matter* **21**, 084203 (2009). doi:[10.1088/0953-8984/21/8/084203](https://doi.org/10.1088/0953-8984/21/8/084203)
37. T. Thonhauser, V.R. Cooper, S. Li, A. Puzder, P. Hyldgaard, D.C. Langreth. Van der waals density functional: Self-consistent potential and the nature of the van der waals bond. *Phys. Rev. B* **76**(12), 125112 (2007). doi:[10.1103/PhysRevB.76.125112](https://doi.org/10.1103/PhysRevB.76.125112)
38. G. Román-Pérez, J.M. Soler. Efficient implementation of a van der waals density functional: application to double-wall carbon nanotubes. *Phys. Rev. Lett.* **103**(9), 096102 (2009). doi:[10.1103/PhysRevLett.103.096102](https://doi.org/10.1103/PhysRevLett.103.096102)
39. S.L. Dudarev, G.A. Botton, S.Y. Savrasov, C.J. Humphreys, A.P. Sutton. Electron-energy-loss spectra and the structural stability of nickel oxide: an LSDA+U study. *Phys. Rev. B* **57**(3), 1505–1509 (1998). doi:[10.1103/PhysRevB.57.1505](https://doi.org/10.1103/PhysRevB.57.1505)
40. R.F.W. Bader, W.H. Henneker, P.E. Cade. Molecular charge distributions and chemical binding. *J. Chem. Phys.* **46**(9), 3341–3363 (1967). doi:[10.1063/1.1841222](https://doi.org/10.1063/1.1841222)
41. W. Tang, E. Sanville, G. Henkelman. A grid-based bader analysis algorithm without lattice bias. *J. Phys.: Condens. Matter* **21**(8), 084204 (2009). doi:[10.1088/0953-8984/21/8/084204](https://doi.org/10.1088/0953-8984/21/8/084204)

Electronic Structure of Metal Phthalocyanines on
Ag(100)

Krull, C.

2014, XVII, 146 p. 81 illus., 54 illus. in color., Hardcover

ISBN: 978-3-319-02659-6